



Effects of preparation method on the microstructure and photocatalytic performance of $\text{ZnSn}(\text{OH})_6$

Xianliang Fu ^{a,b,*}, Danwei Huang ^a, Yong Qin ^a, Longfeng Li ^a,
Xiaoliang Jiang ^a, Shifu Chen ^{a, **}

^a College of Chemistry and Material Science, Huaibei Normal University, Huaibei 235000, Anhui, China

^b Fujian Provincial Key Laboratory of Photocatalysis – State Key Laboratory Breeding Base, Fuzhou University, Fuzhou 350002, China

ARTICLE INFO

Article history:

Received 28 August 2013

Received in revised form

18 November 2013

Accepted 23 November 2013

Available online 1 December 2013

Keywords:

Zinc hydroxystannate

Photocatalysis

Preparation method

Microstructure

ABSTRACT

It is indispensable to find a suitable preparation method to optimize the photocatalyst performance. Different $\text{ZnSn}(\text{OH})_6$ (ZHS) were prepared by four methods in this report, including grinding, coprecipitation, self-templating, and hydrothermal processes. The crystal structures, optical properties, thermal stabilities, and morphologies of the ZHS samples were investigated systematically. Photocatalytic degradation of methyl orange (MO) and gaseous benzene (C_6H_6) over the samples were assessed and compared. The relationship between the microstructure and the photocatalytic performance of ZHS was analyzed. The results reveal the surface microstructure and the photocatalytic performance of ZHS are more sensitive to the preparation methods than the crystal structure and the morphology. A harsh preparation condition leads to the formation of some OH-unsaturated Zn and Sn atoms due to the susceptible of OH groups, which result in a tail light absorption of ZHS and are assumed as the photoactive center. ZHS prepared by the PVP-assisted hydrothermal method exhibits the highest thermal stability, optical absorption, BET surface area and ability for O_2 activation, and consequently shows the highest photocatalytic activity and stability for the degradation of MO and gaseous C_6H_6 .

© 2013 Elsevier B.V. All rights reserved.

1. Introduction

Previous works were mainly focused on the design, preparation, and application of metallic oxides owing to their stability, unique properties, and versatile applications. However, metallic hydroxides have received much less attention for a long time probably because of their instability. The situation has changed somewhat and increasing attentions have been paid to hydroxides recently for some special and promising applications were disclosed as anion exchangers, adsorbents, and catalysts [1–5].

Zinc hydroxystannate ($\text{ZnSn}(\text{OH})_6$, ZHS) is a class of perovskite-structured hydroxide [6]. The metal ions in the hydroxide are octahedrally coordinated with OH to form $\text{Sn}(\text{OH})_6$ and $\text{Zn}(\text{OH})_6$ polyhedra which then connect each other through the O corners to form face-centered-cubic (FCC) crystal structure. Due to its economical, safety, and high effective flame- and smoke-retardant properties, ZHS has been mainly used as additives in

halogen-containing polymeric materials to instead of the conventional toxic Sb_2O_3 [7]. Some other potential applications of ZHS were also developed in recent years. For example, using as a gas sensor for HCHO detection [8], as an antibacterial material against *Escherichia coli* [9], and as photocatalysts for pollutants removal. Among them, one of the most promising applications is in photocatalysis. Recently, we first reported that ZHS can serve as a photocatalyst to effectively degrade of gaseous benzene (C_6H_6) [10], a typical and major indoor air pollutant, and photocatalytic reforming of ethanol to H_2 and CH_4 [11]. Motivated by these works, some other photocatalytic activities of ZHS, including degradation of methyl orange [12], cyclohexane [12], phenol [13], and deconstruction of nitrogen monoxides (NO) [14], were further explored by others. Furthermore, ZHS can be readily transformed to versatile ZnSnO_3 and Zn_2SnO_4 by a simple thermal decomposition procedure, which have drawn a great deal of attentions in dye-sensitized solar cells [15], gas sensors [16], negative electrode material for Li-ion battery [17], and photocatalysis [18].

Owing to its wide potential applications, considerable efforts have been devoted to effectively synthesize ZHS. Including coprecipitation [19], sonochemical [6], mechanochemical [14], hydrothermal [12,20], and solvothermal [10] have been developed for ZHS preparation. In addition, to tailor ZHS for some particular applications, shape-controlled synthesis of ZHS such as cubes,

* Corresponding author at: College of Chemistry and Material Science, Huaibei Normal University, Huaibei 235000, Anhui Province, China.

Tel.: +86 561 3806611; fax: +86 561 3090518.

** Corresponding author. Tel.: +86 561 3806611; fax: +86 561 3090518.

E-mail addresses: fuxiliang@gmail.com (X. Fu), chshifu@chnu.edu.cn (S. Chen).

hollow cubes, truncated cubes, and octahedrons were achieved by adjusting the using amount of NaOH [9,13,21]. These works indicated ZHS could be readily prepared and the structure, formation process, and the morphologic feature of ZHS were investigated routinely. However, the effects of preparation method on the microstructure and the application performance such as the photocatalytic activity of ZHS have rarely been addressed. Taken TiO₂ as example, extensive works indicated its structure, morphology, and photocatalytic performance are highly related to the preparation method [22]. It is reasonable to believe that ZHS would show similar dependency. In fact, this dependency can be perceived in some reported works [10,12,21] because the described photocatalytic performances are quite different. Thus, finding a suitable preparation route to optimize the photocatalytic activity of ZHS becomes indispensable.

Based on the above consideration, different ZHS samples were prepared in this study by four different methods, including grinding, co-precipitation, self-templating, and hydrothermal processes. The crystal structures, optical properties, thermal stabilities, and morphologies of the synthesized samples were characterized systematically. Photocatalytic degradation of methyl orange (MO) and gaseous benzene (C₆H₆) over the samples were evaluated and compared. According to the results, the effects of the preparation methods on the microstructures and the photocatalytic performances of ZHS were finally elucidated.

2. Experimental

2.1. Chemicals and preparation of ZSH

Zinc acetate dihydrate (Zn(Ac)₂·2H₂O), tin chloride pentahydrate (SnCl₄·5H₂O), ZnCl₂, sodium hydroxide (NaOH), Polyvinyl pyrrolidone (PVP, molecular weight 24,000), citric acid monohydrate (C₆H₈O₇·H₂O), and MO were purchased from Sinopharm Chemical Reagent Co. Ltd. All of the chemicals were of analytical grade and used as received. The spin trap 5,5-dimethyl-1-pyrroline-N-oxide (DMPO) was purchased from Sigma Chemical Co.

Different ZHS samples were prepared by grinding, co-precipitation, self-templating, and PVP-assisted hydrothermal methods, respectively, according to the reported procedures or slight modifications thereof. For the grinding route [14], 1.28 g SnCl₄·5H₂O, 0.8 g Zn(Ac)₂·2H₂O, and 1.0 g NaOH were added into an agate mortar and were ground for 30 min. The resulted mixture was then transferred into 150 mL H₂O and was stirred vigorously for 30 min to remove impurity ions. The precipitates were then collected by centrifugation. The product was washed thoroughly with repeating this process several times. A control sample was also prepared by a similar route without grinding the reactants, i.e. via a simple co-precipitation process. For the self-templating route [13], 10 mL mixed aqueous solution of ZnCl₂ (1.0 mmol) and C₆H₈O₇·H₂O (1.0 mmol) was added to 5 mL SnCl₄·5H₂O anhydrous ethanol solution (1.0 mmol), then 10.2 mmol solid NaOH and 25 mL H₂O was added successively into the mixture solution. After stirring for 10 min, 20 mL 2.0 M NaOH solution was added dropwise to the resulted solution and stirring for another 10 min. The formed precipitates were collected by centrifugation and rinsed thoroughly with deionized water. For the hydrothermal method, 0.50 g of SnCl₄·5H₂O, 0.19 g ZnCl₂, and 0.5 g PVP were put into a 50 mL PTFE vessel containing 20 mL H₂O and stirred vigorously for 30 min to form a clear solution. 20 mL 0.5 M NaOH solution was then added dropwise to the solution under stirring. After stirring for a further 60 min, the container with the obtained white slurry was transferred into a stainless steel autoclave and hydrothermally treated at 130 °C for 20 h. The final product formed after the treatment was obtained by centrifugation and rinsed thoroughly with

deionized water and ethanol. All of the samples were dried in air at 90 °C for 10 h before characterization. For convenience, the samples prepared by the grinding, co-precipitation, self-templating, and PVP-assisted hydrothermal methods were labeled as S-a, S-b, S-c, and S-d, respectively.

2.2. Material characterization

The crystallographic information of the prepared ZHS was obtained with X-ray diffraction (XRD) of Cu K α radiation $\lambda = 1.5406 \text{ \AA}$ (Bruker D8 Advance). The UV-vis optical absorption spectra (UV-vis DRS) were recorded on a Shimadzu UV 3600 UV-Vis-NIR spectrometer with BaSO₄ as reference. Multipoint Brunauer-Emmett-Teller (BET) specific surface areas were measured by N₂ adsorption (in relative pressure range from 0 to 0.3) at 77 K on a Micromeritics Tristar II 3020 surface area analyzer. The morphologies of the samples were examined using a field emission scanning electron microscopy (SEM) (FEI Nova NanoSEM 230) and a transmission electron microscopy (TEM) (Hitachi H-800). X-ray photoelectron spectroscopy (XPS) analysis was conducted on an ESCALAB 250 photoelectron spectroscopy (Thermo Fisher Scientific) at $3.0 \times 10^{-10} \text{ bar}$ using Al K α X-ray beam (1486.6 eV). All binding energies were referenced to the C 1s peak of the surface adventitious carbon at 284.8 eV. Photoluminescence (PL) emission spectra of prepared ZHS (0.15 g) were recorded on a JASCO FP-6500 type fluorescence spectrophotometer excited by 254 nm light at room temperature. FTIR spectra of the ZHS were recorded on a Thermo Nicolet Nexus 6700 FT-IR spectrophotometer using KBr pellets in the range 4000–400 cm⁻¹. Thermo gravimetric analysis (TGA) and differential thermal analysis (DTA) measurements were carried out in air at a heating rate of 4 °C min⁻¹ in the temperature range 0–800 °C with a Shimadzu DTG-60H TG/DTA instrument. Electron spin resonance (ESR) signals of radicals spin-trapped by DMPO were recorded at ambient temperature on a Brucker ESR 300 E spectrometer to examine the formation of active radicals over the ZHS samples. All freshly prepared solutions were mixed directly before transferring into a cylindrical quartz cell (length 100 mm, diameter 2 mm). A spot UV-light source of Hamamatsu LC8 (254 nm, equipped with a narrow-bandpass filter) was used in situ as a photo-excitation light source. The ESR signals of the spin adducts, mainly DMPO-·OH and DMPO-O₂^{·-}, were measured in anaerobic ZHS water suspensions and aerobic ZHS methanol suspensions. The spectra were recorded every 20 s. The settings for the ESR spectrometer were as follows: center field 3512.0 G;

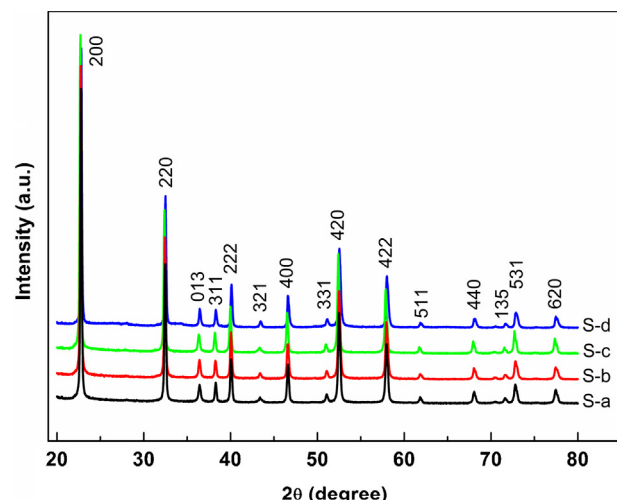


Fig. 1. XRD patterns of the prepared ZHS samples.

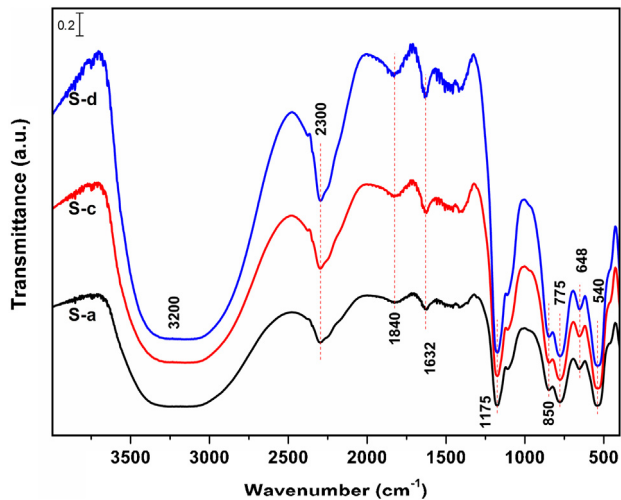


Fig. 2. FTIR spectra of the prepared ZHS samples.

sweep width, 80 G; microwave frequency, 9.85 GHz; modulation frequency, 100 kHz; power, 2.0 mW.

2.3. Photocatalytic measurements

The activities of ZHS were first evaluated by photocatalytic degradation of MO solution. The tests were carried out in a 200 mL tubular reactor which surrounded by a water cooling jacket. The reactor was enveloped by aluminum foil and the jacket was connected to a Julabo F12 heating/cooling bath (Julabo Labortechnik, Germany) to control the reaction solution temperature at about 20 °C by circulating water. A 9 W H-shaped low pressure mercury

UV lamp (Philips TUV PLS-9w, with a monochromatic wavelength emission at 254 nm and intensity ca. 22 $\mu\text{W cm}^{-2}$ (at a distance of 1 m)) was used as the light source. The lamp was assembled at the center of the tubular reactor. In a typical experiment, 100 mg ZHS was first dispersed in 200 mL, 20 ppm MO aqueous solution in an ultrasonic bath to form a suspension. The suspension was then magnetically stirred for 30 min before irradiation to establish an adsorption–desorption equilibrium between ZHS and the reactants. The solution was continuously ventilated with air at a rate of 20 mL min^{-1} throughout the whole reaction. During the experiment, a 3 mL solution was withdrawn through a pipette every 20 min followed by a centrifugation at 10,000 rpm for 3 min. The residual concentration of MO in the filtrate was monitored through a spectrophotometer (Shimadzu UV 3600 UV-Vis-NIR Spectrometer) and used to calculate the decoloration efficiency. The experimental error was estimated within 5% by repeating runs.

Photocatalytic degradation of gaseous C_6H_6 was performed in a fixed-bed tubular micoreactor with a continuous flow mode. The reactor made of quartz tube with length of 250 mm and inner diameter of 4 mm, which was surrounded by four 6 W UV lamp (TUV 6W/G6 T5, Philips, with a wavelength emission at 254 nm and irradiation power of 1.7 W). The schematic diagram of the reaction system is shown in Fig. S1 (Supporting information). In a typical experiment, 0.3 g ZHS was first mixed thoroughly with 3.0 g 50–70 mesh high purity quartz sands (as support material), and then the mixture was loaded into the reactor. Benzene vapor diluted in a pure oxygen stream (250.2 ppm, supplied by a gas cylinder) was used as the reactant stream. The flow rate of the mixture gas was kept at 30 mL min^{-1} by a gas flow controller. Before turning on the lamps, the photocatalyst was purged by the mixture gas at least 3 h to establish an adsorption equilibrium (ca. 250 ± 15 ppm). Simultaneous determination of the concentrations of C_6H_6 and the formed CO_2 were performed on an online gas chromatograph (Agilent

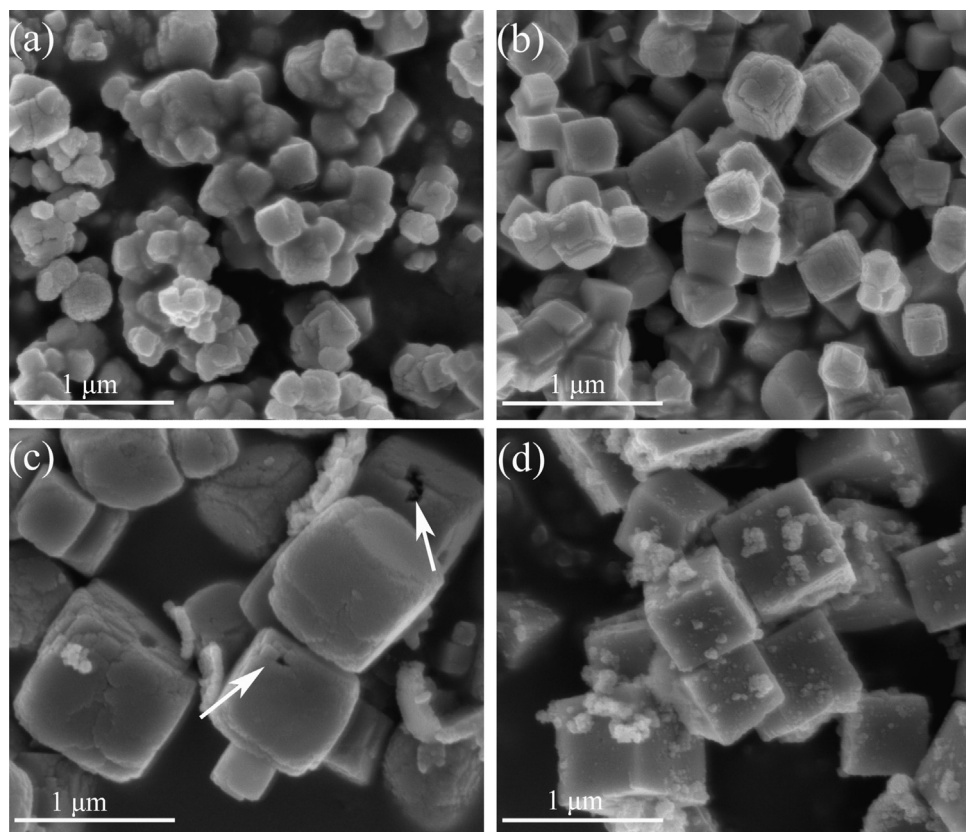


Fig. 3. SEM images of the as prepared (a) S-a, (b) S-b, (c) S-c, and (d) S-d.

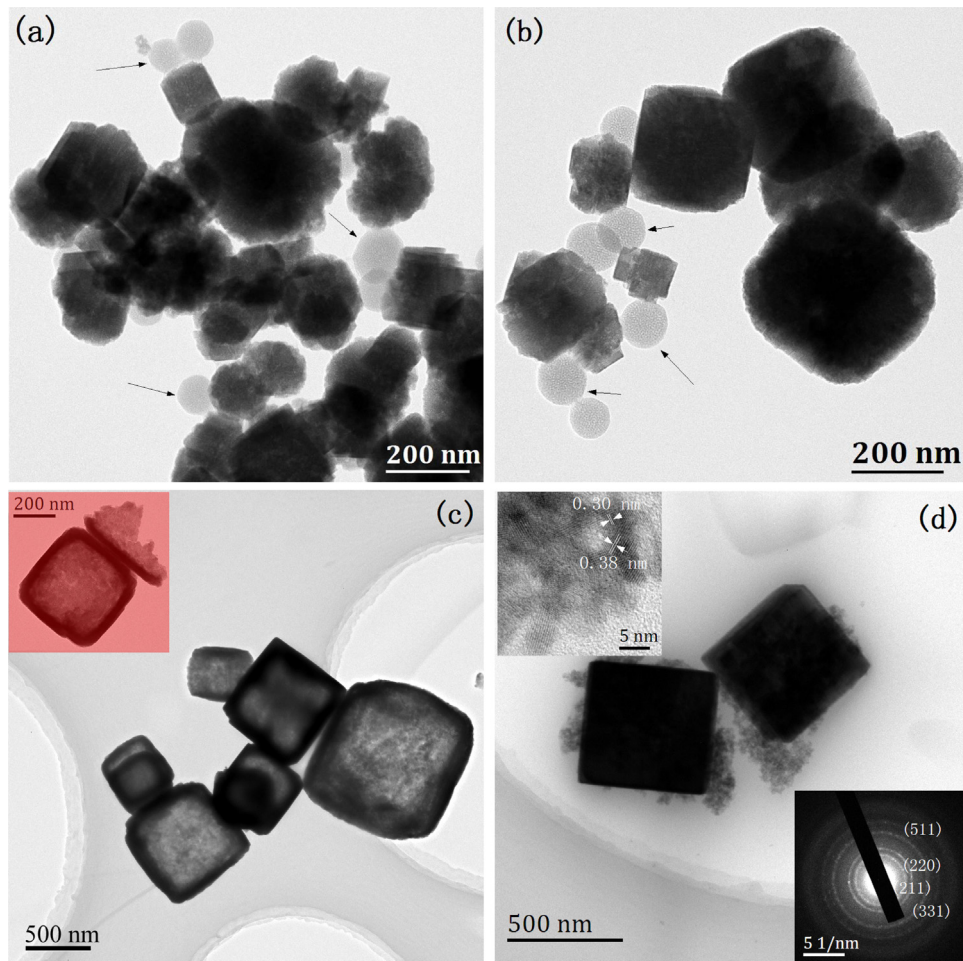


Fig. 4. TEM images of the as prepared (a) S-a, (b) S-b, (c) S-c, and (d) S-d. The inserts of (d) show the HRTEM image of S-d (top) and the corresponding SAED (bottom).

7820A) with a flame ionization detector and a thermal conductivity detector, respectively. During the reaction, the heat generated by the UV lamps was removed by a suction fan and the reaction temperature was controlled at ca. 30 °C.

3. Results and discussion

The XRD patterns of the ZHS samples are shown in Fig. 1. No significant difference was observed. All of the diffraction peaks can be indexed as the cubic phase of $\text{ZnSn}(\text{OH})_6$ (JCPDS 073–2384) with a cell edge of 7.80 Å and a space group of Pn3m. The narrow and strong diffraction peaks of ZHS suggest the phase of ZHS are well crystallized. Thus, it can conclude that ZHS could be successfully synthesized by any of the aforementioned methods. However, caution should be required that some impurity phases such as amorphous ZnO and $\text{Zn}(\text{OH})_2$ may exist due to the covering up of the strong diffraction of ZHS. These components will be disclosed later by the TEM (Fig. 4) and XPS results (Fig. 8).

FTIR spectroscopy can also provide some structural and surface information about the prepared ZHS. The FTIR spectra of S-a, S-c, and S-d are shown in Fig. 2. As S-b prepared by a similar procedure to that of S-a, its spectrum is almost identical to S-a and the result is not shown here. All the samples exhibit similar IR features and quite resemble to the reported $\text{MSn}(\text{OH})_6$ ($\text{M} = \text{Cu, Mg, Zn}$) [6,23]. Thus, the formations of ZHS can be further confirmed here by the FTIR result. An intense broad band centers at about 3200 cm^{-1} together with a sharp absorption at 1175 cm^{-1} is observed, which can be attributed to the stretching vibration ($\nu_{\text{OH str}}$) of the O–H groups in

ZHS or surface adsorbed H_2O [6,24] and the –OH bending vibration ($\nu_{\text{OH bend}}$) of $\text{M}–\text{OH}$ [23,25], respectively. In the $[\text{Sn}(\text{OH})_6]$ polyhedra, the bending of $\text{M}–\text{OH}$ has been reported around 1172 cm^{-1} [25]. Moreover, the OH in-plane deformation vibration and the $\text{H}_2\text{O}–\text{H}_2\text{O}$ hydrogen binding absorption are also observed at 1632 and 775 cm^{-1} , respectively [23,26]. Two vibrations of Sn involved

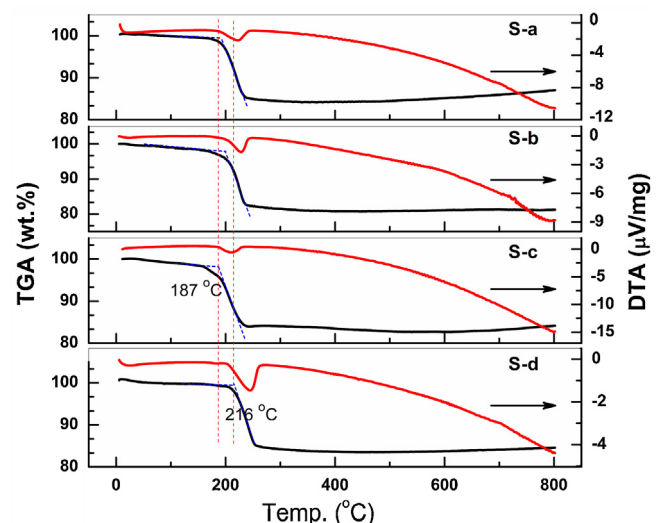


Fig. 5. TGA and DTA curves of the as-prepared ZHS samples.

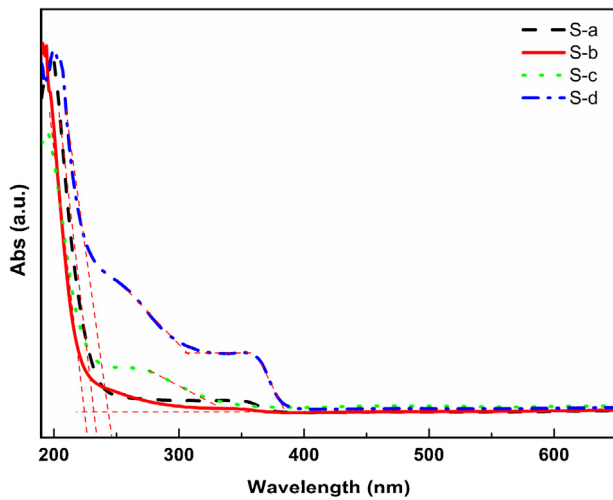


Fig. 6. UV-vis DRS of prepared ZHS samples.

bonds can be found at 540 and 648 cm^{-1} which can be assigned to the stretching modes of Sn–OH, and Sn–O–Sn respectively [23,24,26]. The absorption at around 2300 cm^{-1} is due to the asymmetric stretching vibration of atmospheric CO_2 or adsorbed CO_2 on the ZHS samples [27]. In addition, the spectral bands at 1840 and 850 cm^{-1} which may arise from surface carbonate species formed by the adsorbed CO_2 with H_2O are also noted [28].

The morphology and structural details of the prepared ZHS were investigated by SEM, and TEM techniques. Fig. 3 shows the SEM images of the samples. Due to their intrinsic structures have cubic

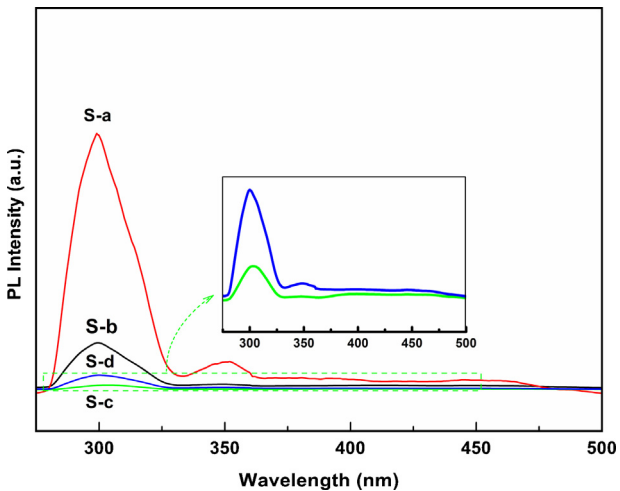


Fig. 7. PL emission spectra of the prepared ZHS samples with excitation light of 254 nm at room temperature.

symmetry, the samples are largely composed by cubic particles except S-a. As shown in Fig. 3a, both spherical and cubic particles with size range of 80–250 nm could be observed in S-a. The less uniform particles aggregate tightly to form a rough surface. For S-b, more uniform cubic particles with size around 280 nm are observed (Fig. 3b). Compared to S-a, the surface of S-b is even, but less compact. Some apparent cracks and terraces can be distinguished on the surface. From the different morphological characteristics between S-a and S-b, it can deduce that the grinding process accelerates the nucleation and the growth of ZHS. Except the grinding process,

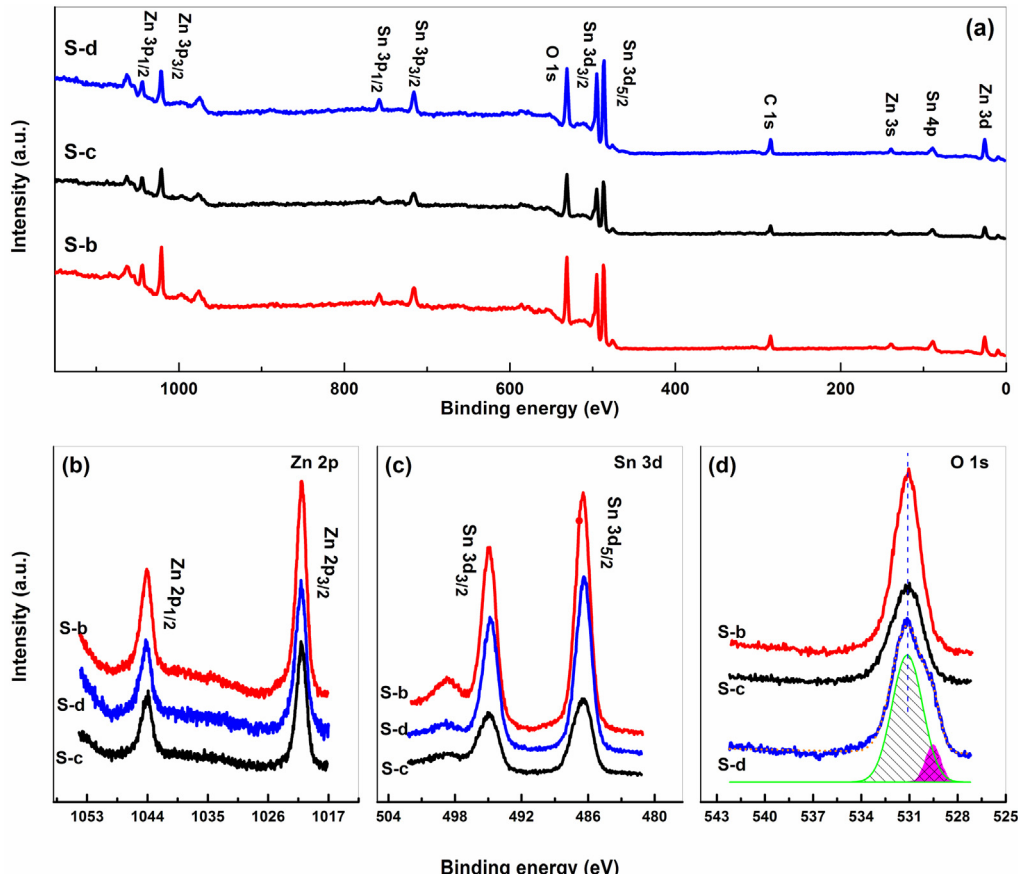


Fig. 8. (a) Survey and high resolution XPS spectra of (b) Zn 2p, (c) Sn 3d, and (d) O 1s for the selected ZHS samples.

the formation of S-a is further promoted by the exothermic effect caused by the interaction of solid NaOH with crystal water containing in the reactants. The combination of these two effects leads to the formation of un-uniform particles in S-a and their aggregation. However, similar problems are inconspicuous for S-b which prepared by a similar process only without grinding, i.e. via co-precipitation route. The average size of the cubic particles in S-c is ca. 600 nm. A close examination reveals that the particles have a hollow structure. As indicated by the arrows in Fig. 3c, some openings on the glossy surface can be observed. The wall thickness of the cubes is about 70 nm as indicated by the broken pieces. The specific formation process of this hollow structure has been well addressed by Wang et al. [13]. As shown in Fig. 3d, S-d composes of uniform, mono-dispersed solid cubic particles with side length ca. 400 nm. However, quite different from other ZHS samples, the cubes in S-d are covered by plenty of small particles which has also been observed in the ZHS sample prepared by solvothermal process in our previous work [10].

The morphology characteristics of the ZHS samples observed in Fig. 3 are further confirmed by TEM and some new features are revealed as well. As shown in Fig. 4a and b, some spherical particles (indicated with arrows) which have a quite different electron density contrast from other particles are observed in S-a and S-b. The XPS result (shown in Fig. 8c, see below) indicated these spheres may be amorphous ZnO or Zn(OH)₂ which formed by the facile hydrolysis of Zn(Ac)₂ in basic solution. The contrast between the dark shell and the pale center further indicates the cubes in S-c have hollow interiors (Fig. 4c). Although the exterior surface of the cubes is smooth, a clear grain boundary can be found inside (inserting in Fig. 4c) suggesting the empty cubes are formed due to an interior etching process induced by NaOH [13]. As shown in Fig. 4d, the cubes in S-d have perfect profile with very clear boundaries. The angle between two adjacent facets is 90° suggesting the cubes are enclosed by six equivalent {100} crystal planes [9,21]. Numerous nanocrystals with sizes ca. 5 nm attach on the cubes surface, which is consistent with the SEM observation (Fig. 3d). Two sets of lattice planes of 0.38 and 0.30 nm are observed in HRTEM image (insert at the top of Fig. 4d), which correspond to (2 0 0) and (2 1 1) planes of cubic ZHS, respectively. It should be noted that, after careful checking of the ICDD database, we found no any phase of ZnO or SnO₂ shares similar *d*-spacing values. The selected area electron diffraction (SAED) pattern (inset at the bottom of Fig. 4d) taken around the small nanocrystals exhibits sharp diffraction rings, revealing the surface grains are randomly oriented. The *d*-spacing of the rings are 0.33, 0.27, 0.18, and 0.15 nm which can be attributed to (2 1 1), (2 2 0), (3 3 1), and (5 1 1) panels of ZHS nanocrystallines, respectively.

The BET surface areas of prepared ZHS were measured by N₂ adsorption at 77 K. The results are 9.9, 1.9, 0.8, and 20.9 m² g⁻¹ for S-a, S-b, S-c, and S-d, respectively. Due to the substantial contribution of the numerous nanocrystals (observed in Figs. 3d and 4d), S-d exhibits the highest BET surface area, even though the cubes length in S-d is larger than that in S-a and S-b (as shown in Figs. 3 and 4). Surprisingly, the surface area of S-c is only 0.8 m² g⁻¹ and much smaller than the reported value [13]. This may due to the fact that the hollow cubes prepared here are considerably larger and thicker (with average length ca. 600 nm and thickness 70 nm, Figs. 3c and 4c) than the reported sample (with length ca. 400 nm and thickness 20 nm). Furthermore, unlike S-d, the important contributor to the surface area, i.e. the small particles, are not found in S-c.

The thermal decomposition properties of the synthesized ZHS were investigated by TGA and DTA. The resulted curves are shown in Fig. 5. As indicated in the TGA curve, a continuous and weak weight loss ca. 1 wt% from room temperature to 120 °C is observed for all ZHS samples. It is caused by the release of physically

adsorbed water from ZHS. Further increasing the temperature, a sharp decrease in mass occurs at ca. 180 °C and ends at ca. 250 °C due to the loss of water upon ZHS decomposition (as indicated by Eq. (1)). The decomposition temperatures of the samples are estimated by the intersection of the extrapolated local horizontal baseline and the tangent to the curve at its steepest point [29]. It indicates the decomposition temperatures decrease in the sequence of S-d (216) > S-b (200) > S-a (192) > S-c (187 °C). The temperatures are close to the reported values [30,31]. S-d presents the highest thermal stability and the decomposition temperature is higher than the lowest one (S-c) about 30 °C. The morphologic features displayed in Figs. 3 and 4 account for this difference because S-d is solid and more compact than other samples, while S-c is hollow and the wall is thin. The total weight losses at 400 °C are calculated to be 15.7, 19.1, 16.6, and 16.4% for S-a, S-b, S-c, and S-d, respectively. Along with the decomposition of ZHS, an abroad endothermic peak corresponding to the dehydroxylation of ZHS is observed for each sample around 250 °C. Further increasing the temperature from 400 to 800 °C, no noticeable weight loss and endothermic or exothermic peak are observed.



After excluding the contribution of the physically adsorbed water (ca. 1 wt%), the weight losses of prepared ZHS caused by their breakdown are less than the theoretical value of 18.9% calculated based on Eq. (1). This suggests some of Zn and Sn atoms are not fully coordinated with OH groups and the corresponding Zn(OH)₆ and Sn(OH)₆ octahedra are not well developed (can be described as M(OH)_x, M=Zn, Sn, x<6). A similar phenomenon has been described by Han et al. [8]. For some Zn atoms in forms of amorphous ZnO or Zn(OH)₂ in S-a and S-b, these components also account for their small weight loss. However, a question then arises, why S-a shows a stronger weight loss deviation than S-b? Considering the different of their preparation route, The most plausible explanation is the impurity component in S-a and S-b is ZnO and Zn(OH)₂, respectively. For S-a, the grinding process accompanied by the exothermic effect favors the generation of ZnO, while for S-b, the co-precipitation route occurred in aqueous media precedes the formation of Zn(OH)₂. Thus, the weight loss deviation of S-b can be partially made up by the presence of Zn(OH)₂. In addition, another possibility is that S-b is better developed than other samples.

The UV-vis DRS of prepared ZHS samples are plotted in Fig. 6. Although the crystal structure and the FTIR absorption features of the ZHS are almost the same, the UV-vis DRS results are quite different. All the samples exhibit an intense absorption threshold at 230–245 nm with steep edge, which can ascribe to the band gap transition of ZHS [8,10]. Due to the different coordination environment of O, the charger transfer transition from O²⁻ to metal ions in hydroxides is larger than their corresponding oxides and generally occurs in the deep UV region, such as In(OH)₃ [32] and GaOOH [33]. Meanwhile, a distinct tail absorption extending to near 400 nm can be observed for all samples, especially for S-c and S-d, and the absorption intensity decreases in sequence of S-d > S-c > S-a > S-b. Similar tail absorbance has been observed over ZHS sample prepared by other process [8,10,11]. The sub-absorption of S-d can be further decomposed into two absorption bands which are onset at ca. 390 and 310 nm, respectively. For S-c and S-a, the sub-absorption can be decomposed into one absorption band beginning at 330 and 380 nm, respectively.

The broad and gradual tail absorptions seems arise from the OH-unsaturated Zn and Sn atoms rather than the amorphous ZnO or Zn(OH)₂ because the tail absorbance of S-a and S-b is quite weak than S-c and S-d. Taken the charger transition from O²⁻ to Sn⁴⁺ as example, reported works [34,35] indicated that the transition highly sensitive to the coordination structure of Sn⁴⁺. To further check the validity of this assumption, OH-unsaturated Zn

and Sn atoms were created intentionally by dehydration of 1.5 g ZHS (synthesized by a reported route [8]) at the decomposition temperature of 220 °C for a short time. As clearly shown in Fig. S2, the tail absorption of ZHS can be subsequently improved without apparently affecting the XRD patterns (insert of Fig. S2).

It is highly probable that $M(OH)_x$ were caused by the different preparation routes. Compared with S-b, the slight high tail absorption of S-a indicates the coordination of Zn and Sn atoms with OH groups may hampered by the grinding process. For S-c and S-d, the addition of citric acid and PVP can compete with OH groups to complex with Zn and Sn atoms [13,36]. Although the additives can be removed during the subsequent rinsing process, the small weight loss of S-c and S-d implies that some of these atoms may in form of $M-O-M$, rather than coordinating with OH groups after washing treatment. Because the light absorption occurs near the surface, the DRS spectra suggest the surface microstructures of prepared ZHS are quite different and susceptible to the preparation method.

A heterostructured photocatalyst can be formed in S-a and S-b for the presence of amorphous ZnO and $Zn(OH)_2$. These foreign components can promote the separation of photo-induced charge carriers or, on contrary, accelerate their recombination. PL emission spectrum can be used to investigate the separation efficiency of photo-induced charge carriers since it results from the recombination of the free carriers. To disclose the nature of these components, the PL emission spectra of S-a and S-b were investigated and compared with that of S-c and S-d under the same test conditions. Fig. 7 presents the PL spectra excited by 254 nm light at room temperature. Although the excited light wavelength larger than the intrinsic absorption thresholds of ZHS (at 230–245 nm, Fig. 6), two PL emissions, a stronger one centered at ca. 300 nm and a weak one at 350 nm, are observed for all samples. It suggests, rather than the intrinsic absorption, the tail absorbance accounts for the generation of photo-induced charge carriers. A much higher PL emission than that of S-c and S-d were produced on S-a and S-b, although they show a quite low tail absorbance (Fig. 6). Thus, it can speculate that the recombination of the free carriers are accelerated by ZnO and $Zn(OH)_2$. This is consistent with the general observation that amorphous structure facilitates the recombination of the photo-generated electrons and holes [37–39]. Although S-c and S-d show high absorption intensities at wavelength above 250 nm (Fig. 6, which means more charge carriers can be generated when activated by 254 nm light), only weak PL emissions are observed here implying a slow recombination rate in S-c and S-d. This is an important prerequisite for high photocatalytic performances.

XPS measurements were carried out to investigate the surface composition and identify the chemical status of the constituent elements. The survey XPS spectra (Fig. 8a) of the representative ZHS samples (S-b, S-c, and S-d) reveal that the samples are composed of Zn, Sn, and O besides C which comes from the adventitious carbon from the XPS instrument. For S-d, no N 1s (at ca. 397 eV) is observed indicating PVP has been removed completely by the washing process. The specific high resolution XPS spectra of the elements are shown in Fig. 8b–d. The peaks centered at 1021.0 and 1044.1 eV (Fig. 8b) correspond to $Zn\ 2p_{3/2}$ and $Zn\ 2p_{1/2}$ for Zn^{2+} state, respectively [8]. The strong peaks centered at the binding energy of 494.7 and 486.3 eV in Fig. 8c can be ascribed to $Sn\ 3d_{3/2}$ and $Sn\ 3d_{5/2}$, respectively. The results agree well with the binding energy of Sn^{4+} ion [8,20,40]. In addition, the Zn LMM Auger peak of ZnO locates at 498.5 eV is observed for S-b, demonstrating that some Zn atoms are in the form of ZnO [41,42] or $Zn(OH)_2$ which transforms to ZnO under the high vacuum condition of XPS measurement. As discussed above, the TGA result (Fig. 5) suggests these atoms in S-a and S-b are more likely in the form of ZnO and $Zn(OH)_2$, respectively. However, for S-c and S-d, the peak is obscure. The result agrees well with the TEM observation of amorphous ZnO in Fig. 4. In some reported works [13,43], the Zn LMM Auger peak can be

distinguished in the prepared ZHS, but it was overlooked by the authors. The O 1s spectra are shown in Fig. 8d. The peaks locate at 531.1 eV and are symmetric except S-d. The asymmetric O 1s peak of S-d can be resolved into two peaks by Gaussian and Lorentzian curve fitting, a strong photoelectron signal around 531.1 eV and a small tail around 529.5 eV. The former can be ascribed to the bulk oxygen in ZHS crystalline network (oxygen in $M-OH$ bonds) [13,40,44] while the later may attribute to other oxygen species such as the surface adsorbed O^- , OH^- , or oxygen in the low coordinated Sn or Zn ions (oxygen in $M-O$ bonds, not in $M-OH$) [44,45].

Both liquid–solid and gas–solid photocatalytic reactions were performed to assess the photocatalytic performances of prepared ZHS. Figs. S3 and 9a show the time dependent photocatalytic decoloration process of MO. As shown in Fig. S3, before turning on the lamp, the reaction solutions exhibit almost the same absorption spectra suggesting the prepared ZHS samples have the same adsorption capacity for MO. After illumination for 140 min, about 43% MO is photo-decolorized without using any photocatalyst. It is no wonder to observe the photolysis of MO because high energy UV-C (254 nm) irradiation was used. S-b exhibits the lowest efficiency for MO degradation, slightly larger than the photolysis process, while S-a and S-c have comparable activity. S-d shows the highest efficiency for MO degradation. After illumination for 100 min, the solution becomes colorless. As displayed in Fig. 9b, a first-order linear relationships is observed between $\ln(C_0/C_t)$ and irradiation time t (C_0 and C_t are the concentrations of MO before and after UV irradiation for t min, respectively). The result suggests the degradation process followed pseudo-first-order kinetics. Thus, the apparent reaction rate constant of the ZHS samples can be determined via the slopes of the fitting lines. The values decrease in order of S-d (2.6×10^{-2}) > S-c (8.6×10^{-3}) ≈ S-a (8.4×10^{-3}) > S-b (6.6×10^{-3} min $^{-1}$).

Photocatalytic degradation of gaseous C_6H_6 over ZHS samples was compared. Fig. 10 shows the concentration variations of benzene and the corresponding degradation product of CO_2 as a function of irradiation time. As a comparison, the activity of the support SiO_2 and Degussa P25, a widely used standard TiO_2 photocatalyst, was also investigated. As shown in Fig. 10e, there is no decrease in C_6H_6 concentration over SiO_2 after turning on the lamps. Instead, the concentration increases gradually and reaches an equilibrium value (ca. 250 ppm) after purging with the mixture gas for about 180 min. No CO_2 was detected during the whole illumination time. The results suggest the support material has no photocatalytic activity for benzene degradation. However, as shown in Fig. 10a–d, the destruction of benzene can be achieved over the prepared ZHS samples. After switching on the lamps, the concentrations of benzene drops immediately from 244 to 0.6, 261 to 233, 264 to 247, and 265 to 0.5 ppm for S-a, S-b, S-c, and S-d, respectively. Along with the drops of C_6H_6 concentration, about 920, 105, 55, and 1070 ppm of CO_2 are produced accordingly. The initial conversions of benzene ($[C_6H_6]_{\text{converted}}/[C_6H_6]_{\text{initial}}$) are almost 100% for S-a and S-d, which are dramatically larger than that of S-b (10.7%) and S-c (6.4%). However, with the illumination time prolonged, only S-c and S-d exhibit stable activities and the corresponding mineralization efficiencies ($[CO_2]/(6 \times [C_6H_6]_{\text{converted}})$) of C_6H_6 are 56.5% and 68%. A gradual increase of C_6H_6 concentration and the consequent drop of CO_2 are observed for S-a and S-b (Fig. 10a and b). Taking S-a as an example, the high conversion of benzene can only sustain for 120 min and then decrease quickly from initial 100% to 50% after illumination for 12 h.

Apparently, among the prepared ZHS samples, S-d exhibits the highest conversion and mineralization efficiency of C_6H_6 . More importantly, no indication of inactivation is observed even after illumination for about 24 h. As shown in Fig. 10d, when the UV lamps were turned off, the C_6H_6 concentration recovers the initial value subsequently and no CO_2 can be detected anymore. The result

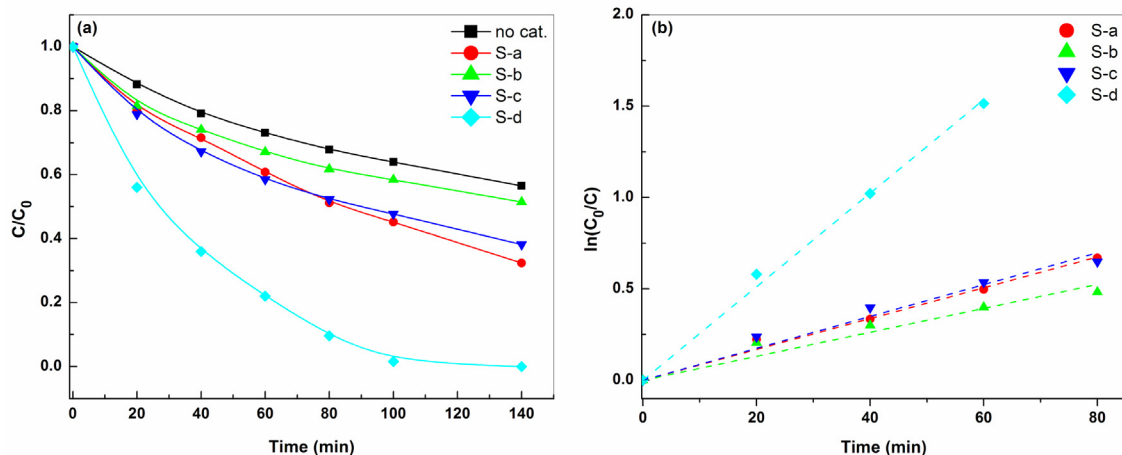


Fig. 9. (a) The temporal changes of MO concentration over prepared ZHS as monitored by UV-vis absorption spectra at 460 nm; (b) Plots of $\ln(C_0/C)$ against degradation time. C_0 and C_t are the concentrations of MO before and after UV irradiation for t min.

further confirms the degradation of C_6H_6 is triggered by the light activated S-d. The discrepancy between the conversion and the mineralization efficiencies observed in S-a and S-d suggests partial of benzene molecules were not degraded completely to CO_2 , but to some other compounds such as CO and formaldehyde [10,46].

Unfortunately, due to the limitation of the analyses conditions, the compounds cannot be detected at present. We believe this problem can be solved by increasing the contact time.

Fig. 10f shows the degradation of benzene on famous P25. The activity of P25 is only comparable to that of S-a. The photocatalytic

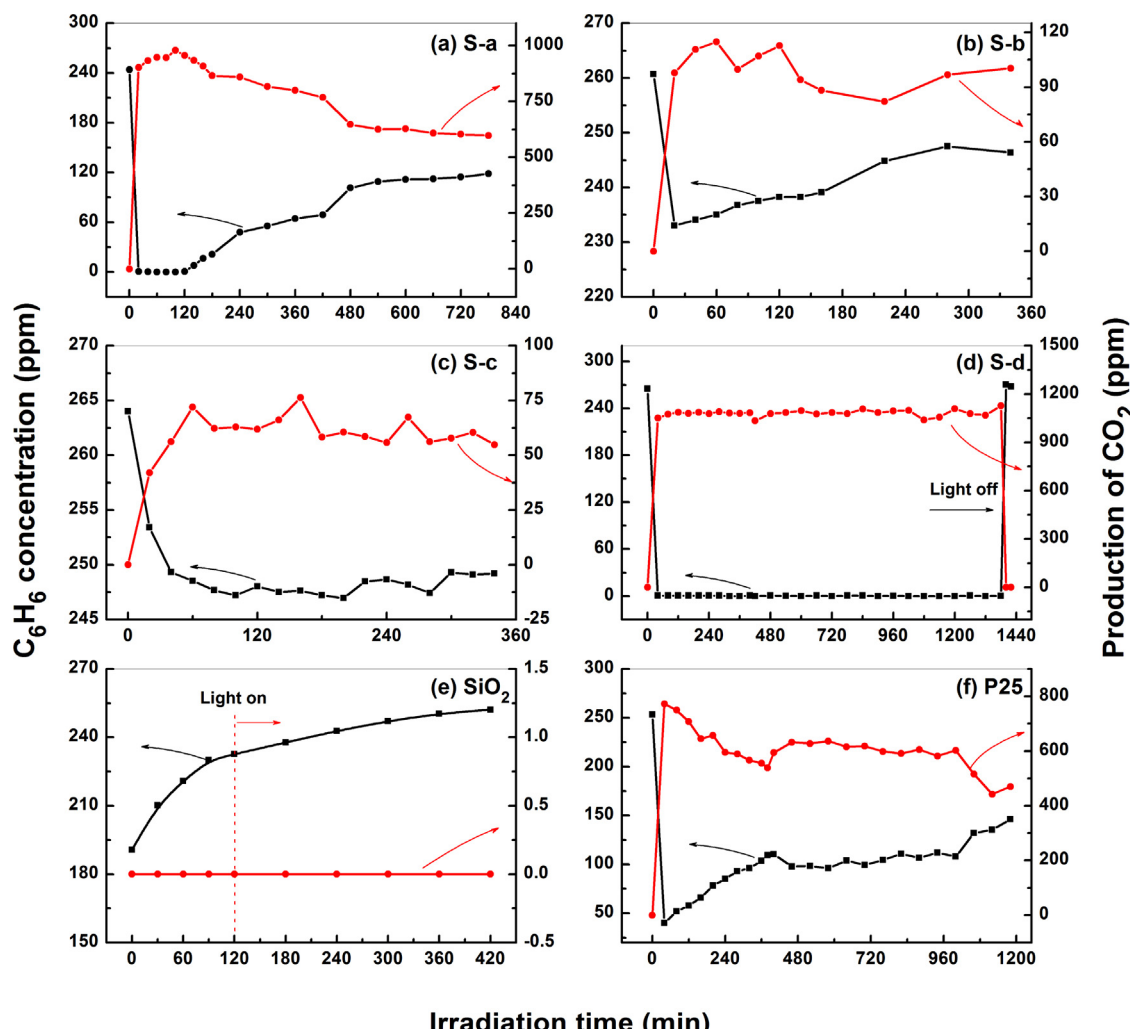


Fig. 10. The variation of C_6H_6 concentration and the corresponding degradation product of CO_2 over (a–d) ZHS samples, (e) SiO_2 and (f) P25 as a function of irradiation time.

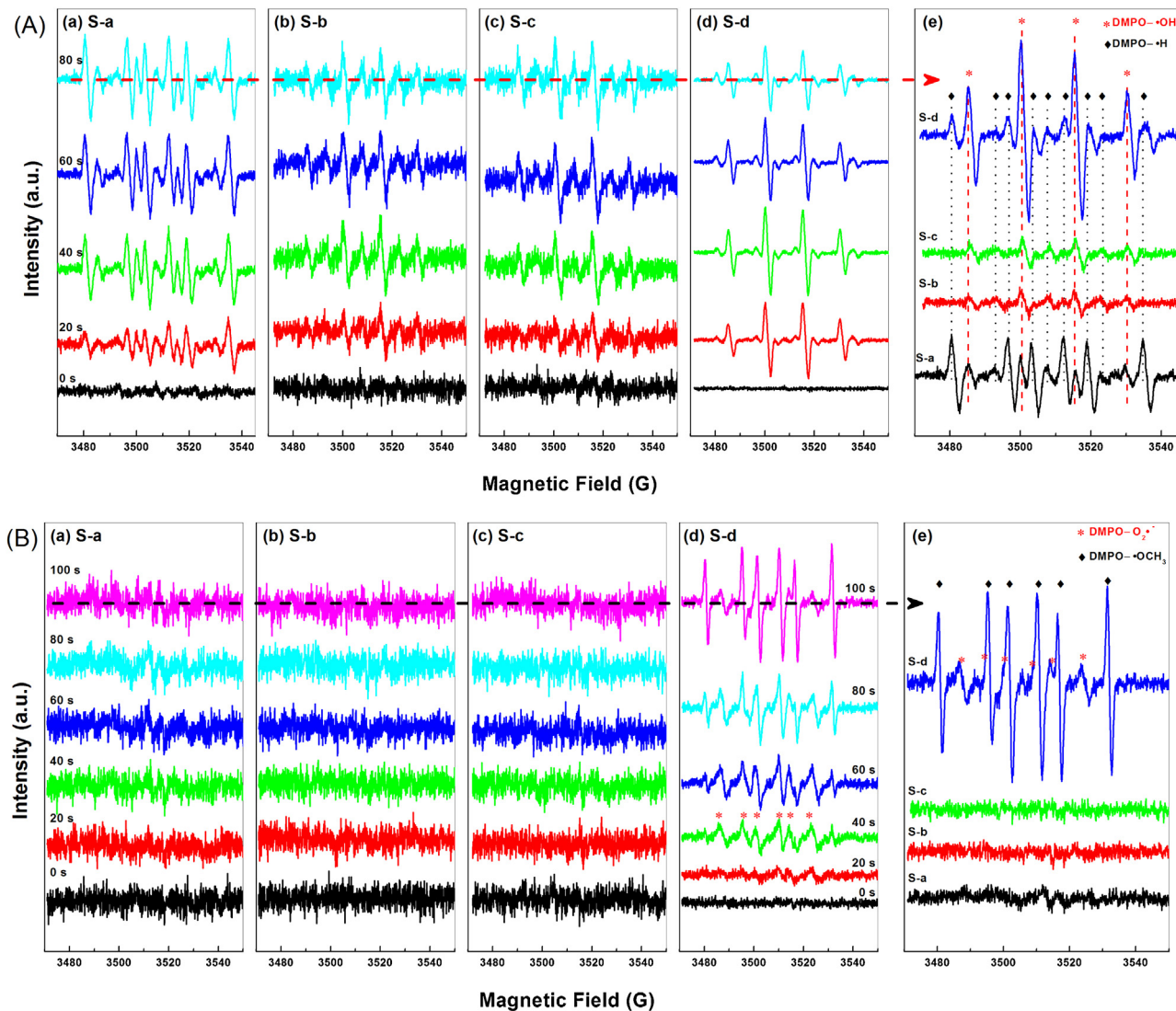


Fig. 11. Temporal changes of the DMPO spin-trapping ESR spectra recorded over ZHS samples at ambient temperature: (A) in aqueous dispersion for $\cdot\text{OH}$ and (B) in methanol dispersion for $\text{O}_2^{\bullet-}$ ($[\text{DMPO}] = 0.20 \text{ M}$, $20 \mu\text{L}$, solvent 0.5 mL , $\text{ZSH} = 10 \text{ mg}$, wavelength of excitation 254 nm).

performance and the stability of P25 are obviously lower than that of S-d. A continuous deactivation of P25 with irradiation time is observed. As shown in Fig. S4, after operation for 20 h, the white P25 turns yellow–brown due to the deposition of some reaction intermediates. Our previous result [10] indicated the intermediates were aromatic compounds which were partially oxidized by the photo-induced oxygen species. We believe the gradual deactivation of S-a and S-b are also caused by these intermediates which are favored by the amorphous ZnO and $\text{Zn}(\text{OH})_2$. However, S-d shows no perceptible color change after illumination for ca. 24 h suggesting the deposition of the intermediates can be ignored.

Hydroxyl radicals ($\cdot\text{OH}$) and superoxide anion radicals ($\text{O}_2^{\bullet-}$) are commonly suggested as the primary oxidizing species in photocatalytic process. To interpret the photocatalytic performances observed over prepared ZHS samples, the generation and evolution of these species with irradiation time were probed by ESR technique with DMPO as a spin trapping agent. Fig. 11A and B shows the temporal changes of the ESR signals of $\text{DMPO}\cdot\text{OH}$ and $\text{DMPO}\cdot\text{O}_2^{\bullet-}$, respectively. As indicated in Fig. 11A, no signals of $\cdot\text{OH}$ adducts can be detected in the dark. After a 20 s illumination, the

characteristic quartet peaks (labeled with * in Fig. 11A–e) of the $\text{DMPO}\cdot\text{OH}$ adduct with intensity ratio ca. 1:2:2:1 can be observed for all water-suspended ZHS samples, which is consist with the reported spectra [10,47]. The intensities of the signals increase gradually with irradiation time (Fig. 11A) indicating the radicals are induced by the UV light. For easy comparison, the signal intensities of $\text{DMPO}\cdot\text{OH}$ formed after illumination for 80 s on the prepared ZHS samples are summarized in Fig. 11A–e. Obviously, S-d and S-a show higher signal intensities (especially S-d) than that of S-b and S-c suggesting a high production of $\cdot\text{OH}$ on S-d and S-a. Except $\text{DMPO}\cdot\text{OH}$, another spin adduct characterized with nine peaks (signed with ♦ in Fig. 11A–e) can be found on S-a and S-d (Fig. 11A–a and b). The most likely candidate for this adduct is $\text{DMPO}\cdot\text{H}$ according to the reported magnetic parameters [48–50]. The formation of $\text{DMPO}\cdot\text{OH}$ and $\text{DMPO}\cdot\text{H}$ can be briefly described in Eqs. (2) and (3), which derive from the oxidation of holes and the reduction of electrons, respectively. For S-d, the signals of $\text{DMPO}\cdot\text{OH}$ is stronger than that of $\text{DMPO}\cdot\text{H}$ (Fig. 11A–d), agree well with the reported works [48,49]. The rapid self-quenching of $\cdot\text{H}$ accounts for this observation. Indeed, H_2 , one of the quench products of $\cdot\text{H}$,

Table 1

Summary the characterization results and the photocatalytic performances of prepared ZHS.

Item	S-a	S-b	S-c	S-d	
Characterization results	DRS*	Weak	Very weak	Moderate	Strong
	TG (wt%)	15.7	19.1	16.6	16.4
	PL	Very strong	Strong	Weak	Very weak
	XPS	No asymmetric O 1s peak was observed	Observed		
	BET ($\text{m}^2 \text{ g}^{-1}$)	9.9	1.9	0.8	20.9
	ESR	Moderate	Weak	Weak	Strong
Photocatalytic activity	MO (min^{-1})	8.4×10^{-3}	6.6×10^{-3}	8.6×10^{-3}	2.6×10^{-2}
	C_6H_6	Moderate, unstable	Low	Low	High, stable

DRS*: the tail absorption.

has been observed over illuminated ZHS in our previous work [11]. However, a contrary phenomenon is observed for S-a (Fig. 11A-a), implying the photo-induced holes cannot be effectively trapped by water to form $\cdot\text{OH}$.



Considering $\text{O}_2\cdot^-$ is unstable in aqueous media [51], the ESR spectra of the DMPO- $\text{O}_2\cdot^-$ was recorded in methanol. Similar data processing procedure is performed as that of DMPO- $\cdot\text{OH}$ and the results are presented in Fig. 11B. Fig. 11B-e compares the final signal intensities of DMPO- $\text{O}_2\cdot^-$ after irradiation for 100 s on the ZHS samples. As shown in Fig. 11B, only S-d exhibits apparent ESR signals (Fig. 11B-d), while the signals on S-a are obscure (Fig. 11B-a). No detectable signal is observed for S-b and S-c even irradiation for 100 s (Fig. 11B-c and d). The six characteristic peaks (labeled with * in Fig. 11B-d) of the DMPO- $\text{O}_2\cdot^-$ adducts formed on S-d could be distinguished after irradiation for 40 s (reaction Eq. (4)). The spectra features resemble our previous findings [10]. The intensities of the peaks increase gradually with the irradiation time in 80 s and then decline with further irradiation. The depletion of the dissolved oxygen and the gradual quenching of $\text{O}_2\cdot^-$ account for this decay. The results indicate, under irradiation, O_2 can only be effectively activated by S-d. Along with the illumination, another adducts signals (labeled with ♦ in Fig. 11B-e) emerge progressively and become prominent 100 s later. The adducts can be assigned to DMPO- $\cdot\text{CH}_2\text{OH}$ [52,53] which originates from the hole oxidation of methanol via Eq. (5).



The photocatalytic reaction involves three processes: the generation of photo-induced charge carriers, the migration of the carriers from bulk to surface, and the interfacial reactions induced by the charge carriers. For a photocatalyst, the efficiencies of these processes are mainly determined by the light absorption, the quantity of recombination sites, the formation of active radicals and the surface area, respectively. The superposition of these factors results in the final photocatalytic activity. As for the prepared ZHS, to reveal the contribution of these factors, the characterization results and the photocatalytic performances of ZHS are summarized and compared in Table 1. The relationship between them is then addressed. The above results indicate the photocatalytic performance of ZHS (Figs. 9 and 10, especially for the degradation of MO) is in proportional to their tail absorption strength (Fig. 6) and inversely proportional to the PL intensity (Fig. 7). It clearly suggests the tail absorbance originated from the unsaturated Zn and Sn atoms rather than the intrinsic absorption accounts for the activity of ZHS. The activity and stability is greatly limited by the quantity of the recombination sites. Furthermore, as summarized in Table 1, the BET surface area is also partially responsible for the photocatalytic

performance, especially the degradation of C_6H_6 . For S-c, there is a discrepancy between the degradation activity of C_6H_6 and the characterization results of DRS and PL. This can be ascribed to its lowest BET surface area (only $0.8 \text{ m}^2 \text{ g}^{-1}$).

Generally, high photocatalytic activity can be expected for the sample with low PL emission intensity [54,55]. However, as indicated in Figs. 9–11, a more consistent relationship between the ESR results and the photocatalytic activity of ZHS such as S-a and S-d can be found. The result suggests using ESR result to indicate the potential photocatalytic activity is more effective and direct than using PL result. This because the generation and the quantities of the oxidizing species which are closely related to the photocatalytic performance can be directly determined by ESR signals. However, the PL result is just an indirect evaluation of the potential activity for it reflects the recombination rate of the free carriers. The ESR result indicates O_2 can only be effectively photo-activated by S-d. This is the key step for the degradation of gaseous C_6H_6 as O_2 is the primary oxidant. The adsorbed oxygen species in S-d (approved by the corresponding asymmetric O 1s peak in Fig. 8) can favor this activation [56,57].

At last, it should be noted that although the OH-unsaturated Zn and Sn atoms are assumed as the photoactive center, their specific structures, contribution to the tail absorbance, and the function during the photocatalytic process are still uncertain and need further investigation.

4. Conclusions

In conclusion, the effects of preparation methods, including grinding, co-precipitation, self-templating, and hydrothermal processes, on the microstructures and photocatalytic performances of ZHS were investigated. The results reveal the XRD, FTIR, and morphology results of the samples are less impacted by the preparation methods. However, due to the susceptible of OH groups, the surface microstructure and the photocatalytic performance are sensitive to the preparation methods. A harsh preparation conditions lead to the formation of some OH-unsaturated Zn and Sn atoms which account for the tail absorption of ZHS and are assumed as the photoactive center. The presence of amorphous ZnO and $\text{Zn}(\text{OH})_2$ are detrimental to the activity. ZHS prepared by the PVP-assisted hydrothermal method exhibits the highest thermal stability, optical absorption, BET surface area, and ability of activation of O_2 , which consequently result in the highest photocatalytic activity and stability for the degradation of MO and gaseous C_6H_6 .

Acknowledgements

This work was financially supported by the Natural Science Foundation of China (NSFC, Grant nos. 21103060, 51172086, and 51272081), the open foundation of Fujian Provincial Key Laboratory of Photocatalysis – State Key Laboratory Breeding Base, Fuzhou

University and the Nature Science Foundation of Anhui Provincial Education Committee (no. KJ2013A231).

Appendix A. Supplementary data

Supplementary data associated with this article can be found, in the online version, at <http://dx.doi.org/10.1016/j.apcatb.2013.11.039>.

References

- [1] M. Meyn, K. Beneke, G. Lagaly, Inorg. Chem. 29 (1990) 5201–5207.
- [2] A.I. Khan, D. O'Hare, J. Mater. Chem. 12 (2002) 3191–3198.
- [3] T. Yan, J. Long, X. Shi, D. Wang, Z. Li, X. Wang, Environ. Sci. Technol. 44 (2010) 1380–1385.
- [4] Z. Li, Z. Xie, Y. Zhang, L. Wu, X. Wang, X. Fu, J. Phys. Chem. C 111 (2007) 18348–18352.
- [5] C. Gomes Silva, Y. Bouizi, V. Fornes, H. Garcia, J. Am. Chem. Soc. 131 (2009) 13833–13839.
- [6] H. Jena, K.V.G. Kutty, T.R.N. Kutty, Mater. Chem. Phys. 88 (2004) 167–179.
- [7] P. Cusack, M. Heer, A. Monk, Polym. Degrad. Stab. 58 (1997) 229–237.
- [8] L. Han, J. Liu, Z. Wang, K. Zhang, H. Luo, B. Xu, X. Zou, X. Zheng, B. Ye, X. Yu, CrystEngComm 14 (2012) 3380.
- [9] J. Yin, F. Gao, C. Wei, Q. Lu, Inorg. Chem. 51 (2012) 10990–10995.
- [10] X. Fu, X. Wang, Z. Ding, D.Y.C. Leung, Z. Zhang, J. Long, W. Zhang, Z. Li, X. Fu, Appl. Catal. B: Environ. 91 (2009) 67–72.
- [11] X. Fu, D.Y.C. Leung, X. Wang, W. Xue, X. Fu, Int. J. Hydrogen Energy 36 (2011) 1524–1530.
- [12] Y. Chen, D. Li, M. He, Y. Hu, H. Ruan, Y. Lin, J. Hu, Y. Zheng, Y. Shao, Appl. Catal. B: Environ. 113–114 (2012) 134–140.
- [13] L. Wang, K. Tang, Z. Liu, D. Wang, J. Sheng, W. Cheng, J. Mater. Chem. 21 (2011) 4352–4357.
- [14] M. Wang, X. Cao, Y. Huang, C. Guo, L. Huang, S. Yin, T. Sato, CrystEngComm 14 (2012) 2950–2953.
- [15] B. Tan, E. Toman, Y.G. Li, Y.Y. Wu, J. Am. Chem. Soc. 129 (2007) 4162–4163.
- [16] I. Stambolova, K. Konstantinov, D. Kovacheva, P. Peshev, T. Donchev, J. Solid State Chem. 128 (1997) 305–309.
- [17] A. Rong, X.P. Gao, G.R. Li, T.Y. Yan, H.Y. Zhu, J.Q. Qu, D.Y. Song, J. Phys. Chem. B 110 (2006) 14754–14760.
- [18] M. Sun, D. Li, Y. Zheng, W. Zhang, Y. Shao, Y. Chen, W. Li, X. Fu, Environ. Sci. Technol. 43 (2009) 7877–7882.
- [19] M. Inagaki, T. Kuroishi, Y. Yamashita, M. Urata, Z. Anorg. Allg. Chem. 527 (1985) 193–202.
- [20] Z. Qin, Y. Huang, Q. Wang, J. Qi, X. Xing, Y. Zhang, CrystEngComm 12 (2010) 4156–4160.
- [21] H. Yu, R. Lai, H. Zhuang, Z. Zhang, X. Wang, CrystEngComm 14 (2012) 8530.
- [22] X. Chen, S.S. Mao, Chem. Rev. 107 (2007) 2891–2959.
- [23] S.-L. Zhong, R. Xu, L. Wang, Y. Li, L.-F. Zhang, Mater. Res. Bull. 46 (2011) 2385–2391.
- [24] J. Kramer, S. Isaacs, V. Manivannan, J. Mater. Sci. 44 (2009) 3387–3392.
- [25] S. Velu, K. Suzuki, M. Okazaki, T. Osaki, S. Tomura, F. Ohashi, Chem. Mater. 11 (1999) 2163–2172.
- [26] N.C. Pramanik, S. Das, P. Kumar Biswas, Mater. Lett. 56 (2002) 671–679.
- [27] C.F. Song, M.K. Lü, P. Yang, D. Xu, D.R. Yuan, Thin Solid Films 413 (2002) 155–159.
- [28] K.D. Dobson, A.J. McQuillan, Langmuir 13 (1997) 3392–3396.
- [29] G.R. Heal, Thermogravimetry Derivative Thermogravimetry, 2002, pp. 10–54.
- [30] G. Wrobel, M. Piech, S. Dardona, Y. Ding, P.-X. Gao, Cryst. Growth Des. 9 (2009) 4456–4460.
- [31] X. Xu, G. Duan, Y. Li, H. Zhang, G. Liu, W. Cai, CrystEngComm 15 (2013) 6159–6164.
- [32] S. Ge, L. Zhang, Environ. Sci. Technol. 45 (2011) 3027–3033.
- [33] M. Sun, D. Li, W. Zhang, X. Fu, Y. Shao, W. Li, G. Xiao, Y. He, Nanotechnology 21 (2010) 355601.
- [34] P. Shah, A.V. Ramaswamy, K. Lazar, V. Ramaswamy, Microporous Mesoporous Mater. 100 (2007) 210–226.
- [35] E.M. Seftel, E. Popovici, M. Mertens, E.A. Stefaniak, R. Van Grieken, P. Cool, E.F. Vansant, Appl. Catal. B: Environ. 84 (2008) 699–705.
- [36] Y. Tang, Y. Jiang, Z. Jia, B. Li, L. Luo, L. Xu, Inorg. Chem. 45 (2006) 10774–10779.
- [37] F. Amano, A. Yamakata, K. Nogami, M. Osawa, B. Ohtani, J. Am. Chem. Soc. 130 (2008) 17650–17651.
- [38] Y. Sakatani, D. Grossi, L. Nicole, C. Boissiere, G.J. de, A.A. Soler-Illia, C. Sanchez, J. Mater. Chem. 16 (2006) 77–82.
- [39] L. Gao, Q. Zhang, Scr. Mater. 44 (2001) 1195–1198.
- [40] M. Mohai, A. Tóth, P.R. Hornsby, P.A. Cusack, M. Cross, G. Marosi, Surf. Interface Anal. 34 (2002) 735–739.
- [41] Y. Zhang, Q. Wang, J. Xu, S. Ma, Appl. Surf. Sci. 258 (2012) 10104–10109.
- [42] Y.-C. Liang, X.-S. Deng, J. Alloys Compd. 569 (2013) 144–149.
- [43] H. Fan, S. Ai, P. Ju, CrystEngComm 13 (2011) 113.
- [44] J.-C. Dupin, D. Gonbeau, P. Vinatier, A. Levasseur, Phys. Chem. Chem. Phys. 2 (2000) 1319–1324.
- [45] H. Zhang, Y. Zuo, Appl. Surf. Sci. 254 (2008) 4930–4935.
- [46] Z.H. Li, Z.P. Xie, Y.F. Zhang, L. Wu, X.X. Wang, X.Z. Fu, J. Phys. Chem. C 111 (2007) 18348–18352.
- [47] Y. Li, B. Wen, C. Yu, C. Chen, H. Ji, W. Ma, J. Zhao, Chem. Eur. J. 18 (2012) 2030–2039.
- [48] F.P. Sargent, E.M. Gardy, Can. J. Chem. 54 (1976) 275–279.
- [49] J. Li, C. Chen, J. Zhao, H. Zhu, J. Orthman, Appl. Catal. B: Environ. 37 (2002) 331–338.
- [50] Q. Chen, H. Shi, W. Shi, Y. Xu, D. Wu, Catal. Sci. Technol. 2 (2012) 1213–1220.
- [51] H. Fu, L. Zhang, S. Zhang, Y. Zhu, J. Zhao, J. Phys. Chem. B 110 (2006) 3061–3065.
- [52] Q. Gu, J. Long, L. Fan, L. Chen, L. Zhao, H. Lin, X. Wang, J. Catal. 303 (2013) 141–155.
- [53] F. Chen, Y. Xie, J. He, J. Zhao, Photochem. J. Photobiol. A 138 (2001) 139–146.
- [54] J.G. Yu, H.G. Yu, B. Cheng, X.J. Zhao, J.C. Yu, W.K. Ho, J. Phys. Chem. B 107 (2003) 13871–13879.
- [55] J. Liqiang, Q. Yichun, W. Baiqi, L. Shudan, J. Baojiang, Y. Libin, F. Wei, F. Honggang, S. Jiazhong, Sol. Energy Mater. Sol. Cells 90 (2006) 1773–1787.
- [56] J. Herrmann, J. Disdier, M.-N. Mozzanega, P. Pichat, J. Catal. 60 (1979) 369–377.
- [57] A. Gurlo, ChemPhysChem 7 (2006) 2041–2052.